



# THE UNIVERSITY *of* EDINBURGH

## Edinburgh Research Explorer

### **Spectropolarimetry of NGC 3783 and Mrk 509: Evidence for powerful nuclear winds in Seyfert 1 Galaxies**

**Citation for published version:**

Lira, P, Kishimoto, M, Goosmann, RW, Campos, R, Axon, D, Elvis, M, Lawrence, A, Peterson, BM & Robinson, A 2021, 'Spectropolarimetry of NGC 3783 and Mrk 509: Evidence for powerful nuclear winds in Seyfert 1 Galaxies', *Monthly Notices of the Royal Astronomical Society* .  
<https://doi.org/10.1093/mnras/stab1751>

**Digital Object Identifier (DOI):**

[10.1093/mnras/stab1751](https://doi.org/10.1093/mnras/stab1751)

**Link:**

[Link to publication record in Edinburgh Research Explorer](#)

**Document Version:**

Peer reviewed version

**Published In:**

Monthly Notices of the Royal Astronomical Society

**General rights**

Copyright for the publications made accessible via the Edinburgh Research Explorer is retained by the author(s) and / or other copyright owners and it is a condition of accessing these publications that users recognise and abide by the legal requirements associated with these rights.

**Take down policy**

The University of Edinburgh has made every reasonable effort to ensure that Edinburgh Research Explorer content complies with UK legislation. If you believe that the public display of this file breaches copyright please contact [openaccess@ed.ac.uk](mailto:openaccess@ed.ac.uk) providing details, and we will remove access to the work immediately and investigate your claim.



# Spectropolarimetry of NGC 3783 and Mrk 509: Evidence for powerful nuclear winds in Seyfert 1 Galaxies

P. Lira<sup>1</sup>, M. Kishimoto<sup>2</sup>, R. W. Goosmann<sup>3</sup>, R. Campos<sup>1</sup>, D. Axon<sup>\*</sup>, M. Elvis<sup>4</sup>,  
A. Lawrence<sup>5</sup>, B. M. Peterson<sup>6,7</sup>, A. Robinson<sup>8</sup>

<sup>1</sup>*Departamento Astronomía, Universidad de Chile, Casilla 36D, Santiago, Chile*

<sup>2</sup>*Department of Astrophysics & Atmospheric Sciences, Kyoto Sangyo University, Kyoto 603-8555, Japan*

<sup>3</sup>*Observatoire Astronomique de Strasbourg, Universit de Strasbourg, CNRS, UMR 7550, 11 rue de l'Universit, F-67000 Strasbourg, France*

<sup>4</sup>*Harvard-Smithsonian Center for Astrophysics, 60 Garden St., Cambridge, Massachusetts 02138 USA.*

<sup>5</sup>*Institute for Astronomy, SUPA (Scottish Universities Physics Alliance), University of Edinburgh, Royal Observatory, Blackford Hill, Edinburgh EH9 3HJ, UK*

<sup>6</sup>*Department of Astronomy, The Ohio State University, 140 West 18th Avenue, Columbus, OH 43210, USA*

<sup>7</sup>*Center for Cosmology and AstroParticle Physics, The Ohio State University, 191 West Woodruff Ave., Columbus, OH 43210, USA*

<sup>8</sup>*Laboratory for Multiwavelength Astrophysics and School of Physics and Astronomy, Rochester Institute of Technology, Rochester 14623, New York, USA*

## ABSTRACT

We present results from high signal-to-noise optical spectropolarimetric observations of the Seyfert 1 galaxies NGC 3783 and Mrk 509 in the 3500–7000 Å range. We find complex structure in the polarized emission for both objects. In particular, Position Angle (PA) changes across the Balmer lines show a distinctive ‘*M*-shaped’ profile that had not been observed in this detail before, but could represent a common trait in Seyfert 1 galaxies. In fact, while this shape is observed in all Balmer lines in NGC 3783, Mrk 509 transitions into a ‘*M*-shaped’ PA profile for higher transitions lines. We have modeled the observed profiles using the STOKES radiative transfer code and assuming that the scattering region is co-spatial with the BLR and outflowing. The results give compelling new evidence for the presence of nuclear winds in these two Seyfert 1 galaxies.

**Key words:** galaxies: Seyfert – galaxies: active – galaxies: nuclei – galaxies: individual: NGC 3783, Mrk 509 – polarization: data and processes

## 1 INTRODUCTION

Arguably, the results from spectropolarimetry of Active Galactic Nuclei (AGN) has been the primary observational evidence that has led to the acceptance of the standard ‘Unified Model’ of AGNs: to a first order, the accretion disk is surrounded by a similarly oriented optically thick dusty torus, with the collimated radio emission being coincident with the system axis. The Broad Line Region (BLR) would also lie within the opaque torus and for Type 1 AGN a direct view of the nuclear source and BLR is only possible in the polar direction. For Type 2 AGNs the BLR can be observed in polarized light, after scattering takes place somewhere in the vicinity of the central source. The position angle (PA) of this polarized emission is generally perpendicular to the radio axis of the source. The rather flat wavelength dependence of the continuum polarization suggests that the nuclear light

is scattered by electrons, while the observed PAs indicate that the scattering occurs somewhere along the throat of a torus, i.e., in the polar directions as seen from the nucleus.

Even Type 1 AGNs sometimes show the same evidence for such ‘polar scattering’ (Smith et al., 2002). However, spectropolarimetric studies of Type 1 AGNs have found that a significant fraction presents continuum position angles which are, to first order, parallel rather than perpendicular to the radio axis of the system, suggesting that besides the ‘polar scatterer’ there is another, much more compact ‘equatorial scattering’ region, that can dominate the polarized spectrum in a significant fraction of Seyfert 1 galaxies (Smith et al., 2002, 2004). An early claim of such equatorial scattering was presented by Antonucci (1984) from the study of polarization in radio galaxies. He argues for a group of objects with ‘parallel’ scattering, referring to the orientation of the polarization PA with respect to the radio jet. In those cases where strong emission lines were detected in polarized light (e.g., 3C 382), Antonucci (1984) notices they

\* Deceased on the 5th April 2012

were significantly broader than any broad component seen in polarized light, and explained it by scattering taking place in a thin disk aligned with the plane of symmetry of the central source.

But, more importantly, the spectropolarimetric results show that in sources with an equatorial scattering region, the polarization PA often rotates significantly across the broad emission lines. This happens for near-field scattering, i.e., with the scatterer being close enough to the H $\alpha$  emitting region to resolve it so that the radiation from the two opposite sides of the, presumably flattened BLR, is scattered at different angles. The early modelling by Smith et al. (2004, 2005) nicely reproduced the sinusoidal PA rotation that characterized the emission lines observed in some sources, although no actual fit to the data was ever attempted until much later (Savić et al. 2018).

As the level of polarization in Type 1 AGN is rather low ( $\sim 1\%$ ), previous studies using 4-meter class telescopes have had a limited number of sources accessible to spectropolarimetry of adequate signal-to-noise. This problem is particularly acute in the blue region of the optical spectrum. We have selected two bright Seyfert 1 galaxies with a known degree of polarization to further study the characteristics of their polarized emission using 8-meter facilities. NGC 3783 and Mrk 509 are two well studied, southern Seyfert 1 galaxies for which emission-line lags for several BLR lines have been measured from reverberation mapping (Reichert et al. 1994; Stirpe et al. 1994; Onken & Peterson 2002, Peterson et al. 2004). Updated black hole masses for both Seyferts can be found in the AGN Black Hole Mass Database (Bentz & Katz, 2015). Hence, *physical* scales for various line emitting regions are available. This is potentially of great importance in understanding the near-field polarization since it could lead to a determination of a physical size for the scatterer and, hopefully, the identification of its nature. Spectropolarimetry of Mrk 509 has already been presented by Goodrich & Miller (1994), Young et al. (1999), Schmid et al. (2000), Smith et al. (2002), and Afanasiev et al. (2019), while previous results for NGC 3783 have been presented by Smith et al. (2002).

## 2 OBSERVATIONS AND DATA REDUCTION

### 2.1 NGC 3783 observations

We observed NGC 3783 ( $z=0.009730$ ) on the 3rd of April 2006 using the FORS1/600B spectropolarimetry mode on the Unit Telescope 2 of the VLT (resolution  $\sim 6 \text{ \AA}$ ), covering the H $\beta$  and higher order Balmer emission lines, and on the 30th of April 1st of May 2006 using EFOSC2/Gr#4 on the 3.6m telescope at La Silla (resolution  $\sim 12 \text{ \AA}$ ), covering the H $\alpha$  emission line.<sup>1</sup>

We implemented sequences of observations consisting of four frames with different waveplate positions (0, 45, 22.5 and 67.5 degrees). The total exposure time was 3.4 hours with FORS 1 and 6.2 hours using EFOSC2. At the VLT, the 1.5'' slit was fixed in the north-south direction, and the

atmospheric dispersion compensator was reset at the start of each sequence. At the 3.6m the slit was approximately parallel to the parallactic angle. No observations were taken at airmass in excess of 1.2.

The CCD frames were bias-subtracted using an averaged bias frame, and flat-fielded using the flat field frames taken with external calibration units during day time. The pixels with obvious cosmic ray hits were fixed using neighboring pixels. There was no need to correct for CCD distortions previous to the spectrum subtraction as o- and e-rays were located close to each other on the detectors ( $\sim 116$  pixels  $\sim 23'' \sim 2.8$  mm for FORS1 and  $\sim 62$  pixels  $\sim 10'' \sim 4.1$  mm for EFOSC2). Inspection of sky lines showed that these had a standard deviation of 0.4 and 0.6 pixels for FORS1 and EFOSC2, respectively, when comparing positions above and below the double spectra and for a wide range of airmasses. Sky subtraction was achieved in the standard way by defining windows on either side of the object spectra. Notice that the individual slits for the o- and e-rays were wide enough to be able to determine the sky level from the same slit where the spectra were found. No residuals were observed at the positions of the sky lines. The sky-subtracted o- and e-ray spectra were combined to produce normalized Stokes parameters  $q$  and  $u$  and the Stokes parameter  $I$ , following Miller, Robinson & Goodrich (1988). The polarization level and position angle,  $p$  and PA, were obtained in the standard way ( $p = \sqrt{(q^2 + u^2)}$ ,  $PA = 1/2 \tan^{-1}(u/q)$ ).  $p$  was also obtained using 'unbiased' prescriptions (Miller, Robinson & Goodrich 1988), but the resulting spectra did not show any significant differences, so the standard definition was finally adopted. The zero point of the polarization signal was checked using the polarized standard star Hiltner 652 ( $p = 6.3\%$  at  $5500 \text{ \AA}$ ) in both runs. The measurement of unpolarized standard stars showed a low instrumental polarization as already reported in previous works (e.g., Fossati et al. 2007, Lamy & Hutsemékers 2000): in the 5200-5800  $\text{\AA}$  range HD94851 gave  $p = 0.07 \pm 0.02\%$  for FORS1 (VLT), while HD97689 gave  $p = 0.02 \pm 0.01\%$  for EFOSC2 (3.6m).

No order-sorting filter was available for the EFOSC2 observations, and thus the measurements at long wavelengths might be slightly affected by a second-order contamination. However we note that the observation of the blue unpolarized star above did not show any systematic polarization at  $\lambda \lesssim 7200 \text{ \AA}$ .

Flux calibration was achieved using the flux standard stars EG274 (VLT), and LTT4816 and Feige67 (3.6m). The data were corrected for Galactic extinction assuming  $E_{B-V} = 0.119$  and using the extinction curve derived by Cardelli, Clayton, & Mathis (1989) with  $A_V/E_{B-V} = 3.1$ .

### 2.2 Mrk 509 observations

We observed Mrk 509 ( $z=0.034397$ ) on the 23th of August 2006 using FORS1 on the UT2 at the VLT. Exposure times were 6.2 and 0.3 hours, for the 600B and 600R grisms (resolution  $\sim 6 \text{ \AA}$  for both settings), respectively. No observations were taken at airmass in excess of 1.5.

Images were reduced in the same manner as described above for NGC 3783. The zero point of the polarization signal was checked using the polarized standard star BD-451133 ( $p = 4.4\%$  at  $5500 \text{ \AA}$ ). The star EGRR 274 was used as the unpolarized standard. The measurement con-

<sup>1</sup> Details of the instrument optical components can be found here <https://www.eso.org/sci/facilities/paranal/instruments/fors/inst/pola.html> and here <https://www.eso.org/sci/facilities/lasilla/instruments/efosc/inst/efosc.html>

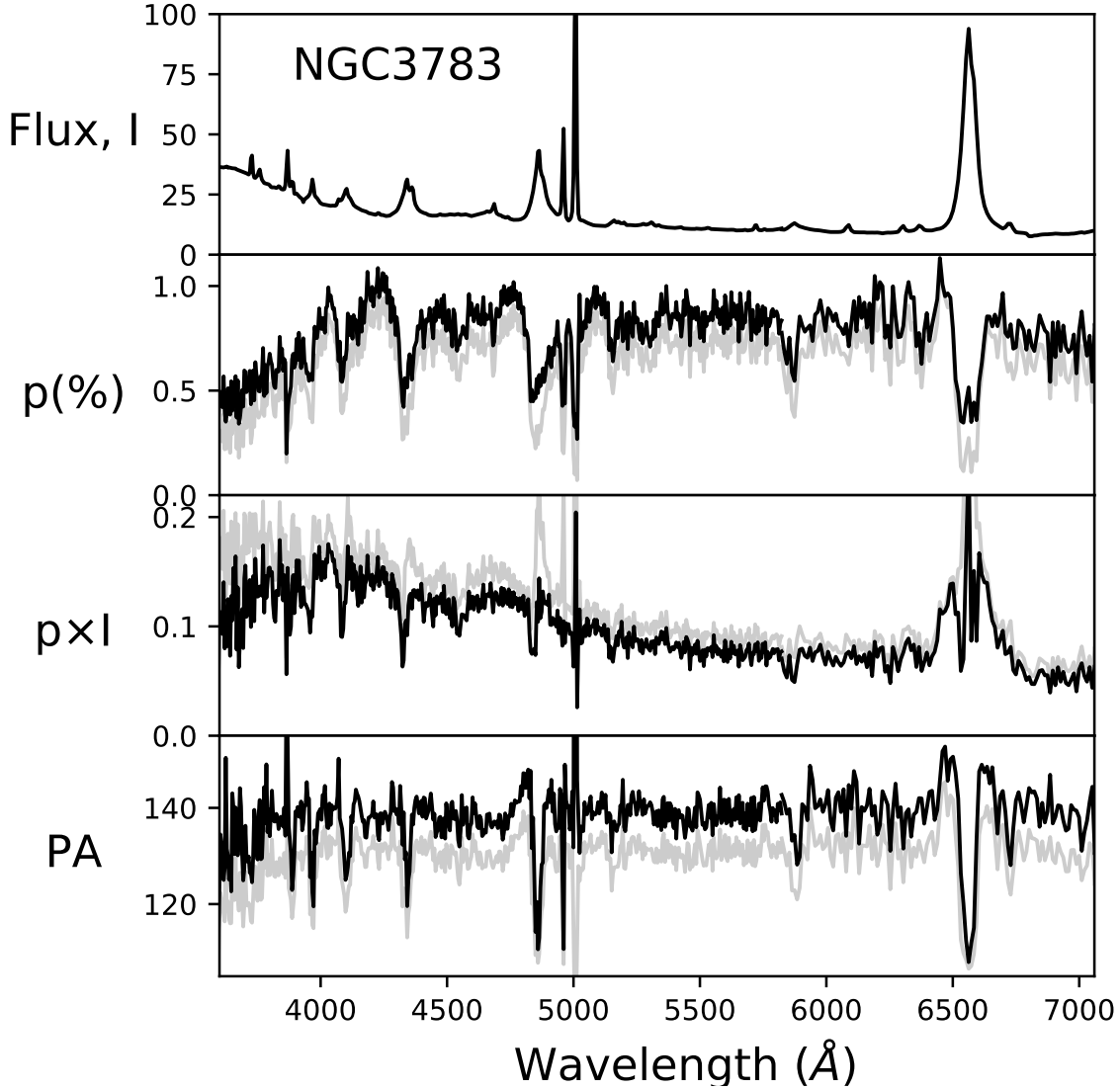


**Figure 1.** Rest-frame spectropolarimetry of NGC 3783. From top to bottom: total flux ( $I$  – in units of  $10^{-15}$  erg/s/cm<sup>2</sup>/Å), degree of polarization ( $p$  – in percentage), polarized flux ( $p \times I$  – in units of  $10^{-15}$  erg/s/cm<sup>2</sup>/Å) and polarization position angle (PA – in degrees). Black spectra correspond to data corrected for intervening ISP polarization, while gray spectra correspond to the data as observed.

firmed the low instrumental polarization at  $p = 0.10 \pm 0.05$  (%) in the 5200–5800 Å range. As before, the data were also corrected for a foreground extinction of  $E_{B-V} = 0.057$ .

### 2.3 Intervening Polarization and Atmospheric Depolarization

An important concern when analyzing polarimetric data is that dust-induced Inter-Stellar Polarization (ISP) along the line of sight to the active nucleus must be taken into account (Hoffman et al., 2005).

To quantify the amount of ISP in our Galaxy towards NGC 3783 ( $b = 23^\circ$ ), we observed a few Galactic stars in the same field. They are close in projection to NGC 3783 and have spectroscopically-determined distances large enough to probe most of the interstellar polarization within the Galactic disk. These observations suggest the Galactic interstellar polarization towards NGC 3783 to be  $\sim 0.25\%$  at PA

$\sim 105^\circ$ . The same exercise along the line of sight towards Mrk 509 ( $b = -29^\circ$ ) gives a Galactic interstellar polarization of  $\sim 0.18\%$  at PA  $\sim 100^\circ$ .

We examined the level of polarization in the OIII lines after ISP correction. For this, it is necessary to first subtract the continuum in the original polarized flux spectra, which was achieved by fitting a low degree polynomial to the data. The results show that the intrinsic polarization of these lines is very low, at  $p \sim 0.001 \pm 0.0003\%$  for NGC 3783 and  $p \sim 0.002 \pm 0.0006\%$  for Mrk 509, in agreement with their noisy appearance in the  $p \times I$  spectra of both sources. This is expected considering that the Narrow Line Region (NLR) is sufficiently large so that geometrical cancellation (this is, the depolarization due to the combination of rather random polarized signals) can be very efficient. This is a good indication that there are no further sources of intervening ISP contamination towards the nucleus of these two galaxies. Corrected and uncorrected observations are presented in

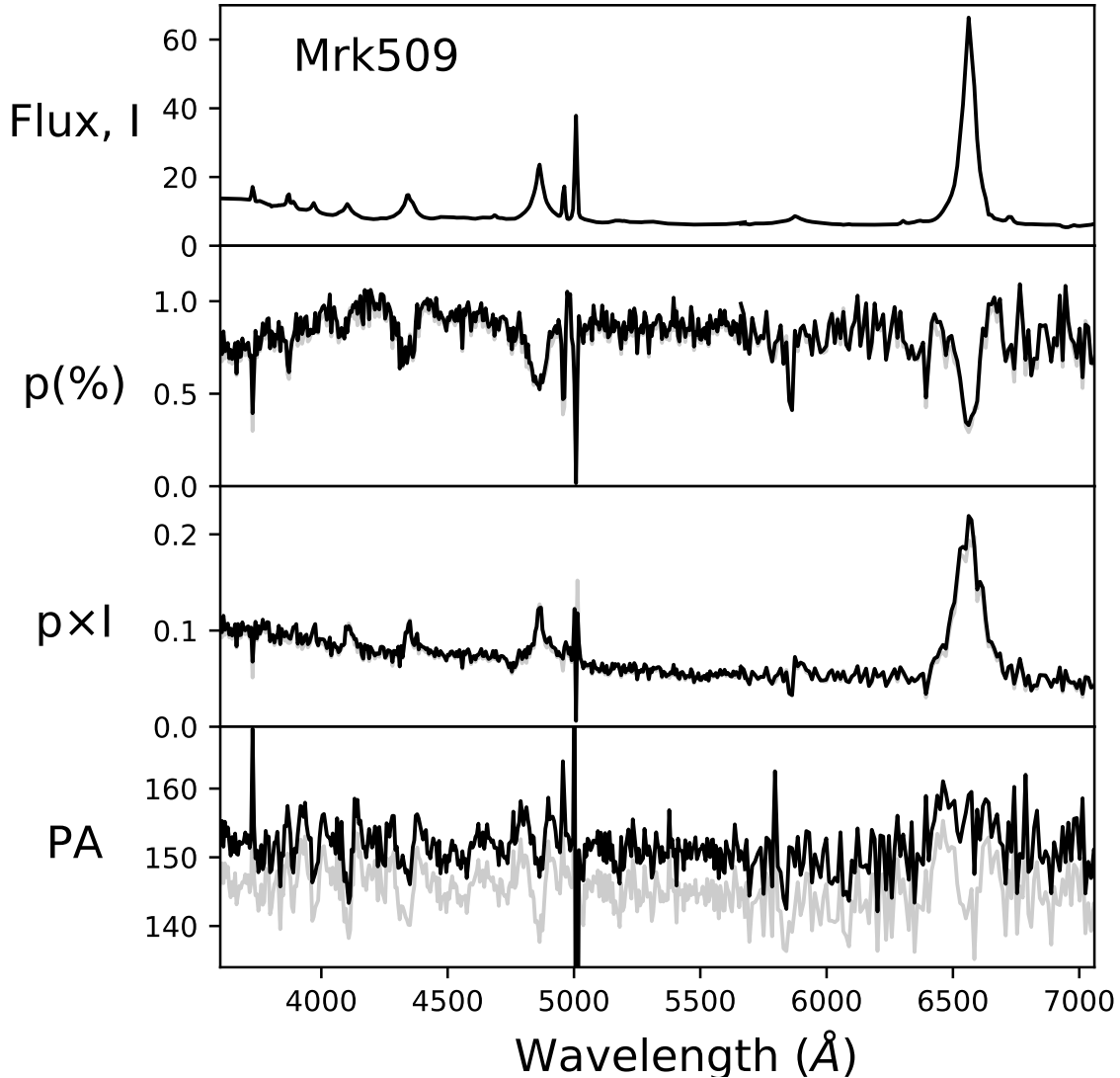


**Figure 2.** Rest-frame spectropolarimetry of Mrk 509. From top to bottom: total flux ( $I$  – in units of  $10^{-15}$  erg/s/cm<sup>2</sup>/Å), degree of polarization ( $p$  – in percentage), polarized flux ( $p \times I$  – in units of  $10^{-15}$  erg/s/cm<sup>2</sup>/Å) and polarization position angle (PA – in degrees). Black spectra correspond to data corrected for intervening ISP polarization, while gray spectra corresponds to the data as observed.

Figures 1 and 2, while unnormalized, ISP-uncorrected Q and U spectra for our sources are presented in the Appendix.

Finally, we also tried to correct for the amount of atmospheric depolarization affecting our observations. As explained by Afanasiev & Amirkhanyan (2012), the atmosphere introduces a variable amount of transmission between consecutive frames, which leads to a time-dependent differential intensity in the o- and e-ray spectra. As shown by Afanasiev & Amirkhanyan (2012) the time scale for these changes is about 30 min and appears as low amplitude oscillations in the Stokes spectra. As repeated visits to our sources correspond to about the same time scale (cycling through four frames with different waveplate positions in order to determine the Stokes vectors, with individual exposures of 400 and 500 seconds for NGC 3783 and Mrk 509, respectively), it was not feasible to correct for this effect. However, as we will show in the next section, the amplitude of the features observed in the spectra of NGC 3783 and Mrk 509 are not only large and abrupt, but also they clearly

coincide with the presence of emission lines in the spectra and have common patterns (see also the Q and U Stokes parameters presented in the Appendix), therefore demonstrating that they must be intrinsic in nature.

### 3 RESULTS

Figures 1 and 2 show the total flux ( $I$ ), degree of polarization ( $p$  – in percentage), polarized flux ( $p \times I$ ) and polarization position angle (PA) obtained from our observations of NGC 3783 and Mrk 509, before and after applying the corrections for polarization along the line of sight detailed in Section 2.3. In what follows we will discuss the main results from the ISP corrected observations.

### 3.1 Common Features

The median value of the corrected PA spectra gives important information about the location of the scatterer medium when it can be contrasted with information about the geometry of the systems. In Figure 3 we show the mean PA obtained through our spectropolarimetric observations and the projected axis of symmetry of the systems as obtained from dynamical evidence for NGC3783 (Fischer et al. 2013) and radio observations for Mrk509 (Singh & Veestergard, 1992). In both cases we see that the angles are almost aligned, confirming that these two objects are dominated by equatorial scattering.

Our observations of both Seyfert 1 galaxies also show that the degree of continuum polarization  $p$  is essentially flat above  $\sim 4000 \text{ \AA}$  arguing that electron scattering is responsible for the observed polarization. The  $p$  spectra also show strong decrements at the position of the core of the emission lines, indicating that the lines have a lower fraction of polarized flux than the continuum. There is also evidence, particularly clear in the case of NGC 3783, that the broad Balmer lines are flanked by high polarization shoulders coincident with the line wings. This is similar to what is found in other Seyfert galaxies, where the broad line components seem more polarized than the surrounding continuum (e.g., Schmid et al., 2000), resulting in broader emission lines in polarized flux, as has been already discussed by Goodrich & Miller (1994) and Young et al. (1999) for the case of Mrk 509.

As observed by Young et al. (1999) the lower polarization at the line cores is indicative of an intrinsic lower polarization or of polarization at a significantly different position angle. To explain this further, consider the intensity of the polarized continuum and line flux as  $f_{\text{cont}}$  and  $f_{\text{line}}$ , respectively. Then for a  $\Delta\text{PA} \sim 0^\circ$ ,  $p \times I \sim f_{\text{cont}} + f_{\text{line}}$ ; but if  $\Delta\text{PA} \sim \pm 90^\circ$ , then  $p \times I \sim \pm(f_{\text{cont}} - f_{\text{line}})$ . For  $0 < \Delta\text{PA} < \pm 90^\circ$ , intermediate cases would be found<sup>2</sup>. Hence, depolarization occurs for  $\Delta\text{PA} \neq 0$ , and therefore it is a direct consequence of a different spatial distribution of the emitting and/or scattering regions<sup>3</sup>. Our observations clearly show that depolarization strongly affects the broad components of the emission lines.

PA rotation across the broad lines has long been recognized as common in Seyfert 1 galaxies (Miller & Goodrich, 1994; Young et al., 1999; Schmid et al., 2000; Smith et al., 2002, 2004) and Afanasiev et al. (2019) recently published a compilation of spectropolarimetric data for 30 Seyfert 1 galaxies showing H $\alpha$  PA rotation from which black hole masses were derived. We observe PA rotation in both, Mrk509 and NGC3783 and will discuss the details in Sections 3.2 and 3.3.

The lower polarization below  $4000 \text{ \AA}$  seen in Figures 1 and 2 is in striking contrast with the behavior of the continuum observed in direct light, which rises steeply towards the blue in both galaxies. This has not been noticed in other Seyfert 1 galaxies before, although a marginal slope

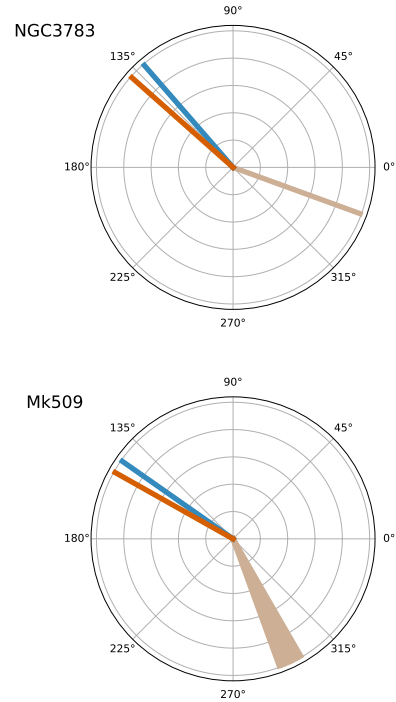


**Figure 3.** Comparison of the mean PA values determined from spectropolarimetry and other methods for our sources. The axis of symmetry of the systems as determined by Fischer et al. (2013) for NGC 3783 and Singh & Veestergard (1992) for Mrk 509, are shown in brown. Position Angles (PAs) derived by our observations are presented in blue (uncorrected values) and orange (corrected by Galactic ISP).

change in  $p$  might be present in previous observations of objects with spectra obtained below  $4000 \text{ \AA}$ : Mrk 376, Mrk 704, I Zw 1 (Goodrich & Miller 1994; Smith et al., 1997), the exception being Fairall 51, whose  $p$  spectrum raises continuously towards the blue (Schmid et al., 2001; Smith et al., 2004).

A similar behavior to that observed in the  $p$  spectra of NGC 3783 and Mrk 509 has already been observed in quasars (Antonucci 1988; Schmidt & Smith et al., 2000; Kishimoto, Antonucci & Blaes, 2003), and has been suggested as due to the presence of ‘small blue bump’<sup>4</sup> (SBB) emission, which can dominate the continuum flux below  $4000 \text{ \AA}$ . The SBB should be polarized in the same way as the BLR, as it appears as direct consequence of the emission line formation processes. Therefore, this pseudo-continuum will depolarize the continuum in the same manner as the broad emission lines, resulting in a lower polarized flux at the blue end of the spectra.

### 3.2 NGC 3783

Essentially no variation was found between the data obtained during our VLT and 3.6m runs, which overlap in the

<sup>2</sup> Note that this happens because the two signals are incoherent, and therefore their sum is *not* the result of the vectorial addition of plain waves, but of their Stokes vectors.

<sup>3</sup> In the modelling presented in Section 4, depolarization will result from the different spatial distribution of the continuum and line emitting regions.

<sup>4</sup> The ‘small blue bump’ corresponds to the Balmer continuum and a blend of higher order Balmer and FeII emission lines (Wills, Netzer & Wills 1985).

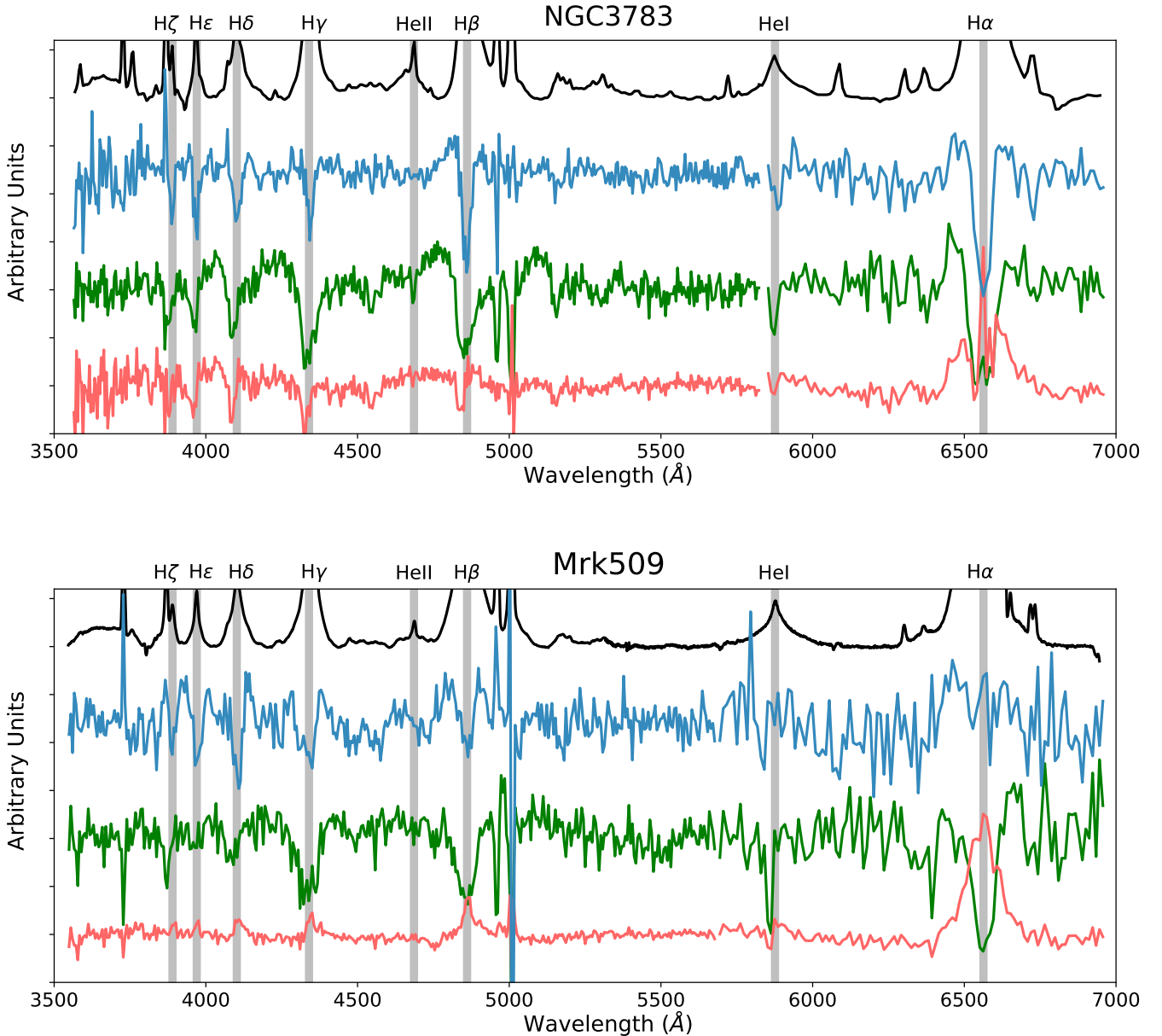


**Figure 4.**  $I$  (black), PA (blue),  $p$  (green), and  $p \times I$  (red) spectra for NGC3783 (top) and Mrk509 (bottom). All spectra have been continuum subtracted to allow for a better inspection of the line features. Vertical lines have been drawn to coincide with the central wavelength of the Balmer and He emission lines.

4060–5870 Å region. Hence, in what follows we directly compare the structure observed in the  $H\alpha$  and  $H\beta$  emission lines obtained in the different runs.

The observed continuum polarization level is clearly higher than that observed by Smith et al. (2002), who reported observations obtained with the AAT. Our data (Apr 2006) show  $p \sim 0.9\%$  at  $\sim 131^\circ$  before ISP correction, while Smith’s observations (May 1997; no ISP correction introduced) show  $p \sim 0.5\%$  at  $\sim 136^\circ$ . After correcting for ISP (see Section 2.3), the mean polarization is found to be  $p = 0.7 \pm 0.1\%$  in the 5300–5600 Å range. The PA spectrum is centered around  $138 \pm 2.5^\circ$ .  $H\alpha$  and  $H\beta$  clearly show a ‘ $M$ -shaped’ PA profile, with very deep central troughs. In higher order Balmer lines, the ‘shoulders’ of the  $M$  feature might however not be present, but the central deep troughs

are still very conspicuous. This peculiar shape had already been seen in the  $H\alpha$  line presented in the work of Smith et al. (2002), who interpreted it as possibly due to the effects introduced by the NII doublet. This is clearly not the case, as we have shown that the NLR shows negligible polarization and the same profile is repeatedly seen in all Balmer transitions.

Figure 4 shows the  $I$ ,  $p$ ,  $p \times I$  and PA spectra for NGC3783 in arbitrary units. All spectra were continuum subtracted using a low-degree spline polynomial fit for better inspection of the emission line features.

The presence of depolarization features at the location of emission lines and the SBB is more clearly appreciated in Figure 4. For example, there seems to be hint of depolariza-



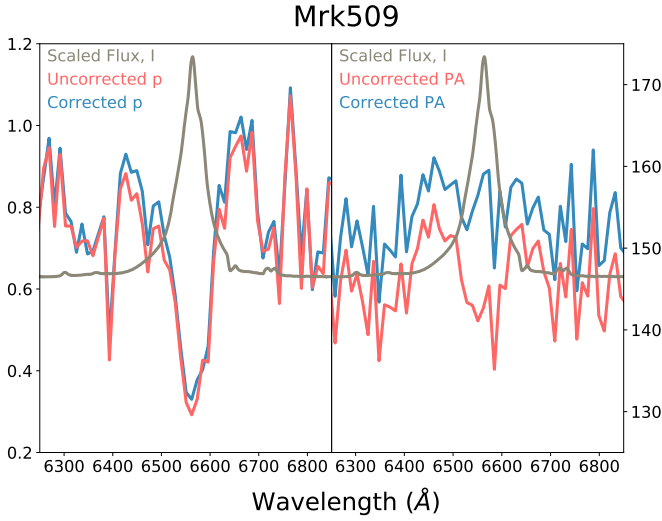


**Figure 5.** ISP corrected and uncorrected  $p$  (left) and PA (right) spectra of Mrk 509 in the  $H\alpha$  spectral region.

tion coincident with the HeII line at 4686 Å, while a much stronger signal is seen for HeI at 5876 Å.

In the  $p \times I$  spectrum the FWHM of  $H\alpha$  is very broad, at  $\sim 220$  Å, almost three times the width of the line seen in total flux. Together with the coincidence of the PA with the projected axis of symmetry of the system, this is confirmation of scattering taking place in the equatorial plane of the system, as the velocity difference between the BLR and scattering material is not diminished by projection effects (Smith et al., 2005). The  $p \times I$  spectrum is also fairly unusual in that the Balmer lines are seen only ‘in absorption’, with the exception of  $H\alpha$ . Clearly, the depolarization in NGC 3783 at the line positions is very strong, suggesting that the lines and the continuum are polarized at very different angles. This is consistent with the very strong PA changes ( $\sim 30^\circ$ ) seen across the lines.

Notice also how the depolarization of the Balmer lines is blue-shifted with respect to the peak position of the lines seen in total flux. This can be seen when comparing the  $p$  and  $p \times I$  spectra presented in Figure 4. The PA troughs, however, are symmetric with respect to line centers.

### 3.3 Mrk 509

For Mrk 509 the  $H\alpha$  and  $H\beta$  spectral regions were observed during the same observing run and therefore can be examined together. The red spectrum is however of low quality, and we present heavily binned data in Figures 2 and 4.

Variability in the scattering properties of Mrk 509 indicates that at least one scattering component corresponds to a compact region, probably located close to the BLR. In fact, Young et al. (1999) showed that the polarization level and position angle in the 4350–7100 Å range present a clear correlation in data compiled from 1985 to 1997, with  $p$  increasing from  $\sim 0.5\%$  at  $\sim 140^\circ$  to  $\sim 0.9\%$  at  $\sim 155^\circ$ , previous to any correction to the polarized signal due to an ISP component. Our uncorrected spectropolarimetric obser-

vations for Mrk 509 with  $p \sim 0.9 \pm 0.1\%$  at  $\sim 145 \pm 2^\circ$  in the 5300–5600 Å range, are in agreement with the previous trend. The ISP corrected values are  $p = 0.86 \pm 0.04\%$  and  $PA = 150 \pm 1^\circ$ .

As with NGC 3783, the  $p$  spectrum of Mrk 509 is characterized by strong depolarization at the position of the emission lines. In the  $p \times I$  spectrum the FWHM for  $H\alpha$  is  $\sim 120$  Å, almost twice the width of the line seen in total flux, as expected for equatorial scattering. Contrary to what is observed in NGC 3783, no strong break is seen in the continuum at wavelengths  $\lesssim 4000$  Å in  $p \times I$  flux shown in Figure 2 and 4, but some flattening is present.

The profiles of the Balmer lines change significantly along the PA spectrum, starting with a slightly asymmetric bump for  $H\alpha$  (the quality of the data does not allow further characterization), to the appearance of a trough at the center of the  $H\beta$  profile, with deeper troughs appearing in higher Balmer transitions. Notice that these troughs cannot be caused by the narrow line components, as it was already established that the polarization level of the NLR is very low. The PA shape for the higher-transition Balmer lines resembles the ‘*M-shaped*’ profile observed in NGC 3783. This is particularly clear in the  $H\gamma$ ,  $H\delta$  and  $He$  transitions. The pattern is, however, more symmetric than in the case of NGC 3783, with the central trough and the shoulders of the *M* feature showing similar amplitudes.

Several previous spectropolarimetric observations of Mrk 509 have been published (Goodrich & Miller 1994, Young et al. 1999, Schmid et al. 2000, Smith et al. 2002, Afanasiev et al. 2019). Of particular particular interest are those by Goodrich & Miller (1994) and Schmid et al. (2000), taken in 1985–1987 and 1999, respectively, because of the high signal-to-noise ratio of the data and because the observations by Goodrich & Miller (1994) extend to the blue and include the  $H\beta$  line.

Since none of the works mentioned above corrected their observations for ISP effects, it is important first to look at the changes introduced by this correction. As can be seen in Figure 2, and in more detail in Figure 5, the ISP correction flattens the PA signal across the  $H\alpha$  emission line, although little change is seen in  $p$ . Figure 2 also shows that the changes in the PA profile shape of the  $H\beta$  line are less significant. Since the PA profile is of particular interest it is safer to refer only to the uncorrected spectra in what follows.

Comparing the PA spectra of Goodrich & Miller (1994), Schmid et al. (2000) and our uncorrected data (gray lines in Figure 2) shows that the blue side of the  $H\alpha$  line is very similar in all three cases: a rise followed by a drop that coincides with the center of the emission line and with a total amplitude of  $\sim 20$ – $25$  degrees. The red side in our data, however, differs from the other two cases, with a second rise centered at  $\sim 6635$  Å that reaches above the continuum level and that is not seen in Goodrich & Miller or Schmid’s spectra. This could be explained by noise, as our data obtained for the red (600R grism) spectrum are of low quality. However, it is also important to notice that a pure equatorial scattering model predicts that the center of the line should coincide with the point where the sinusoidal PA profile crosses the level of the continuum emission (Smith et al. 2005, Savić et al. 2018, Lira et al. 2020), and not with the lowest point of the trough, which is the case of Mrk 509 and seen in all



observations. This is already indication of a departure from the basic equatorial scattering picture.

Besides, the PA spectrum presented in Goodrich & Miller (1994) hints that the  $H\beta$  profile seems different from that seen in  $H\alpha$ , with a narrow drop and wings that quickly rise back to the continuum level on both sides of the line, as it is also the case when inspecting our observations presented in Figure 2.

## 4 MODELLING

Recently, Lira et al. (2020) have explored the BLR polarised signal for different geometrical and dynamical scenarios, and have found that equatorial scattering can give rise to a wide range of PA profiles. In particular, they have been able to obtain profiles similar to those first proposed by Smith et al. (2002, 2004), but also  $M$ -type profiles that resemble those observed in NGC 3783 and Mrk 509. These last models required that 1) the BLR and a scattering media are coincident, 2) both regions undergo Keplerian rotation, 3) the scatterer must be optically thin in the polar direction but offer enough optical depth to photons escaping at low angles with respect to the disk geometry, and 4) the scattering medium presents a significant outflowing velocity.

### 4.1 Exploration of Parameter Space

In this section we will present variations to the modelling carried out in Lira et al. (2020) in order to fit our observations. Essentially, we would like to determine the physical characteristics of the BLR and the scatterer invoking a model that is able to reproduce most of the key aspects of the data, such as the behavior observed in the  $p$  and PA spectra at the location of the BLR emission lines. All models have been obtained using the STOKES software (Goosmann & Gaskell 2007, Marin et al. 2012). Other examples of STOKES modelling and capabilities can be found in Marin et al. (2015), Marin (2018), Rojas Lobos et al. (2018), and Savić et al. (2018, 2020).

One caveat that needs to be explained at this point is that while the BLR is an optically thick emitting source, STOKES does not allow for such structures. Instead, once an emitting source is defined, all its volume is responsible for emitting line photons at random directions. Hence, the anisotropic nature of the emission from BLR clouds (e.g., Pancoast et al., 2014) cannot be incorporated in our models. Furthermore, as the scattering region is required to be optically thin in the polar direction, ultra thin BLR and scattering disks are adopted. This is not a good physical representation of the sources, but it is required by the current limitations of the modelling. A better motivated representation would correspond to optically thick emitting clouds surrounded by a thin atmosphere of outflowing gas.

In Figure 6 we present the PA and  $p$  spectra for several variations of the base model already presented in Lira et al. (2020). The base model consists of what is known for NGC 3783 in terms of its central black hole and the location of the BLR: a  $4 \times 10^7 M_{\odot}$  in mass surrounded by a Keplerian-rotating, thin disk-like BLR. The line emission generated by this BLR is centered at  $6563 \text{ \AA}$  and has an intrinsic width of  $50 \text{ \AA}$  or  $2286 \text{ km/s}$ . The scattering region is coincident

with the BLR, has a density of at least  $5 \times 10^6$  electrons per  $\text{cm}^{-3}$ , and presents Keplerian rotation as well as an equatorial outflowing wind. Crucially, the PA profile from this base model shows a  $M$ -type PA profile, characterized by the peaks and central trough having similar amplitudes (see Lira et al., 2020), which is close to what is seen in the higher order Balmer lines in Mrk 509 but a bad match for the profile seen in NGC 3783, which is characterized by a very deep central trough, and so variations to this base model need to be explored.

In Figure 6, panel **a**, we show that the amplitude of the  $M$  feature is a strong function of the line-of-sight angle ( $i$ ), as the PA is subject to a scaling by a  $\cos(i)$  factor ( $i \sim 0$  corresponds to a face-on disk). The level of polarization,  $p$ , suffers the opposite effect, as a face-on orientation gives a null  $p$  value due to complete geometrical cancellation for a perfectly circular geometry (notice that in panel **a** the  $p$  spectrum for a 54 degree inclination angle is off the plot).

BH mass has a great impact on both, the PA and  $p$  spectra (panel **b** in Figure 6) for a BLR located at the *same physical radius* from the central BH. The PA spectrum develops stronger shoulders for massive BHs, with the redwards shoulder being more prominent. The  $p$  line shape shows a strong asymmetric ‘U’ shape for low BH masses, becoming less prominent and skewed towards the blue for larger BH masses. Notice that the *continuum*  $p$  level remains constant regardless of the BH mass.

Panels **c** and **d** in Figure 6 show that the shape of the PA and  $p$  profiles strongly respond to the radial speeds of the BLR and scatterer. In general terms, as the radial velocity  $v_{\text{rad}}$  of the scatterer increases (panel **c**) the  $M$  profile gets amplified, becoming broader and with larger peaks and troughs. In all cases the continuum  $p$  level remains constant, while at the line position complex, although low-amplitude structure appears. The  $p$  profile develops a  $M$ -type profile for  $v_{\text{rad}} > 3000 \text{ km/s}$ . Notice also how the trough of the  $p$  profile becomes skewed towards the blue for the largest  $v_{\text{rad}}$  value.

Strong changes in PA are also seen for different values of the BLR radial velocity (panel **d** in Figure 6). The profile becomes wide and less deep for negative (inflow) velocities. Likewise, it becomes narrower and deeper for larger outward speeds. Similar trends are seen in the  $p$  spectra.

Panels **e-h** in Figure 6 present the dependency on the disk height, outer radii, and electron density. As can be seen, these changes mostly affect the  $p$  spectra, with only small changes introduced to the PA morphology.

The heights of the BLR and scattering media have a large effect on the observed value of the continuum of the  $p$  spectra. For equal height of both media (panel **e**), the continuum level rises by  $\sim 50\%$  each time the height is doubled (from  $0.001$  to  $0.002$  to  $0.004 \text{ pc}$ ). The ratio between the thickness of the BLR and scattering media shows that while a BLR spatially thinner than the scatterer boosts the  $p$  continuum, the opposite happens when the BLR is thicker than the scatterer (panel **f**). Interestingly, the profile of the line in the  $p$  spectrum shows reduced shoulders in this last case, which seems a closer match to the Mrk 509 data.

It is found that the physical thickness of the disk is somewhat degenerate with the electron density  $\rho_e$  (panel **g**) in that both parameters largely control the level of continuum polarization  $p$  without altering the PA spectrum.

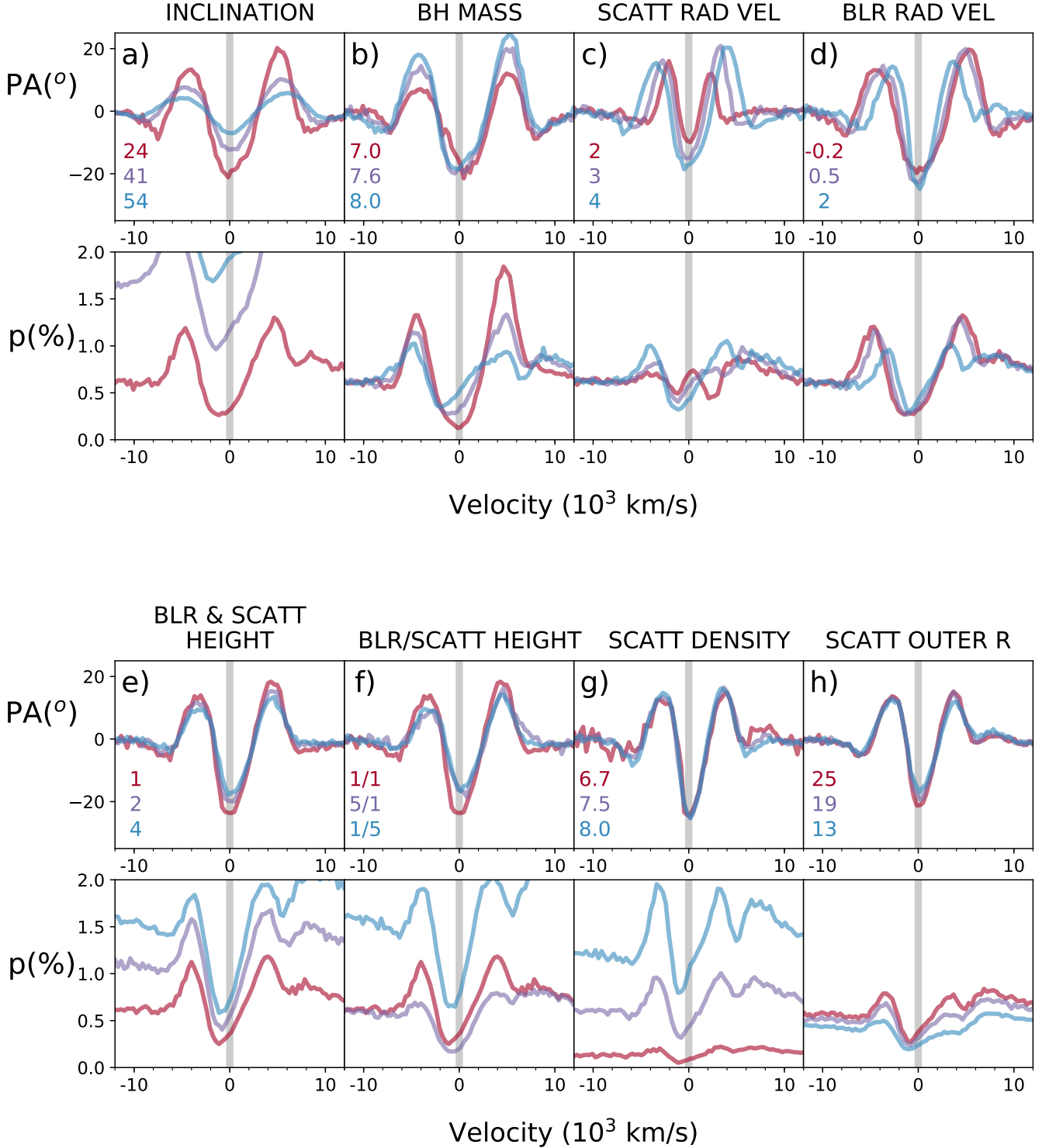


**Figure 6.** Changes in PA and  $p$  spectra as a function of the following model parameters: **a)** inclination (viewing) angle (in degrees; notice that the  $p$  spectrum for the 54 degree inclination is off the plot), **b)** log of BH mass (in  $M_{\odot}$ ), **c)** scatterer radial velocity (in  $10^3$  km/s), **d)** BLR radial velocity (in  $10^3$  km/s), **e)** BLR and scatterer height (in milli-pc), **f)** BLR/scatterer height ratio (in milli-pc), **g)** log of scatterer density (in  $\text{cm}^{-3}$ ), **h)** scatterer outer radius (in milli-pc). Color-coded values are presented in each panel. For further details see Table 1.

**Table 1.** Parameter Values for Figure 6

| Panel | General Parameters  |                                     | BLR Parameters         |                         |               |                                 | Scatterer Parameters   |                         |               |                                   |                                 |
|-------|---------------------|-------------------------------------|------------------------|-------------------------|---------------|---------------------------------|------------------------|-------------------------|---------------|-----------------------------------|---------------------------------|
|       | Inclination<br>degs | $\log M_{\text{BH}}$<br>$M_{\odot}$ | $R_{\text{in}}$<br>mpc | $R_{\text{out}}$<br>mpc | Height<br>mpc | $v_{\text{rad}}$<br>$10^3$ km/s | $R_{\text{in}}$<br>mpc | $R_{\text{out}}$<br>mpc | Height<br>mpc | $\log \rho_e$<br>$\text{cm}^{-3}$ | $v_{\text{rad}}$<br>$10^3$ km/s |
| a)    | <b>24 41 54</b>     | 7.6                                 | 4                      | 30                      | 1             | 0                               | 4                      | 30                      | 1             | 7.5                               | 5                               |
| b)    | 24                  | <b>7.0 7.6 8.0</b>                  | 4                      | 30                      | 1             | 0                               | 4                      | 30                      | 1             | 7.5                               | 5                               |
| c)    | 24                  | 7.6                                 | 4                      | 30                      | 1             | 0                               | 4                      | 30                      | 1             | 7.5                               | <b>2 3 4</b>                    |
| d)    | 24                  | 7.6                                 | 4                      | 30                      | 1             | <b>-0.2 0.5 2</b>               | 4                      | 30                      | 1             | 7.5                               | 5                               |
| e)    | 24                  | 7.6                                 | 4                      | 30                      | <b>1 2 4</b>  | 2                               | 4                      | 30                      | <b>1 2 4</b>  | 7.5                               | 5                               |
| f)    | 24                  | 7.6                                 | 4                      | 30                      | <b>1 5 1</b>  | 2                               | 4                      | 30                      | <b>1 1 5</b>  | 7.5                               | 5                               |
| g)    | 24                  | 7.6                                 | 4                      | 30                      | 1             | 2                               | 4                      | 30                      | 1             | <b>6.7 7.5 8.0</b>                | 5                               |
| h)    | 24                  | 7.6                                 | 4                      | 30                      | 1             | 2                               | 4                      | <b>25 19 13</b>         | 1             | 7.5                               | 5                               |

Changes in electron density, however, introduces strong changes in the line observed in the  $p$  spectrum, with the amplitude of the profile becoming larger for higher values of  $\rho_e$ , and also resulting in the appearance of very strong and sharp shoulders, which is not seen by increasing the BLR and/or scatterer height. Notice also that any structure with a height larger than 0.001 pc will become optically thick in the vertical direction for electron densities above  $\rho_e = 10^8 \text{ cm}^{-3}$ .

The radial location of the scattering medium also impacts the observed profiles, but to a lesser degree. Panel **h** of Figure 6 presents models for a scatterer starting at 0.005 pc and with outer edges at 0.025, 0.019 and 0.013 pc. It shows that the impact in the PA profiles is insignificant, while some changes are observed in the  $p$  spectra. As expected, the larger the overlap between BLR and scatterer, the higher the polarization fraction.

Table 1 summarizes the different parameter values presented in Figure 6. Variations of several parameters, however, do not simply correspond to the combination of the different features shown in Figure 6 as this is clearly a non-linear problem. In particular, it was found that varying velocity radial profiles were needed to properly account for the observed properties when modelling NGC 3783 and Mrk 509 in the following Sections.

## 4.2 Spectropolarimetric modelling of NGC 3783 and Mrk 509

In what follows we will present the best fit modelling obtained for several emission lines observed in polarimetric mode for NGC 3783 and Mrk 509. We will not attempt to give a physical interpretation of how the polarized signal arises as a result of the different adopted parameters, as Lira et al. (2020) showed that the complex nature of these models makes a straightforward analysis a rather difficult task. Instead, we will interpret the best fit parameters in the context of what is already known about these two sources.

The parameter space was explored carefully in order to determine the “best fit” models. Unfortunately, a MCMC procedure was not adopted because of time restrictions given the large number of possible variables and the expense of every single simulation. Instead, we manually tested different parameter combinations after identifying how the models responded to parameter changes, as already shown in Figure 6. The most important observational constraints come from the Reverberation Mapping (RM) results for both

sources, as presented by Onken & Peterson et al. (2002) for NGC 3783 and Peterson et al. (2004) for Mrk 509.

One aspect of the modelling that is important to address now is that different emissivity profiles as a function of radius will be adopted for the different lines in the Balmer series. This seems counterintuitive at first, since all of them are produced by electron recombination to the same ion,  $\text{H}^+$ . However, it is well established that for very high electron and flux densities, as is the case of the BLR, the Balmer lines are not produced under the same physical conditions. This is because the populations of excited states of neutral Hydrogen not only cannot be neglected, but also are proportional to the flux of ionizing photons (e.g., Ferland, Netzer & Shields 1979; Ferland et al. 1992). An important consequence is that different Balmer lines are formed at different distances from the central nucleus, which is clearly demonstrated by reverberation mapping results, with the weighted mean delays for the first three lines in the series found to be  $\tau(\text{H}\alpha):\tau(\text{H}\beta):\tau(\text{H}\gamma) = 1.54 : 1.00 : 0.61$  (Bentz et al. 2010). It is then natural that different emissivity radial profiles are also adopted when analyzing different lines of the Balmer series.

The goodness of the fits were checked applying  $\chi^2$  tests to the features observed in the normalized Stokes Q/I ( $q$ ) and U/I ( $u$ ) data. Using  $q$  and  $u$  instead of the PA and  $p$  is less problematic since it does not suffer from degeneracies,  $p$  being always positive (while  $q$  and  $u$  can be positive or negative) and PA also presenting a sign degeneracy. By normalizing the Q and U spectra by the total intensity I, the results become independent of the brightness of the source (and model, as the strength of the line is given by the number of simulated photons, which is completely arbitrary) and allows to examine only the level of fractional polarized flux. In what follows we present and discuss the best fit results as seen in the  $p$  and PA spectra, but the reader can also find the  $q$  and  $u$  fitting results in the Appendix.

Fits to the data were obtained within  $\pm 15000$  km/s of the line centers, which ensures that the line features as well as the continuum level were properly taken into account. The intrinsic PA value corresponding to the continuum level was subtracted from the PA spectra so that it became consistent with a position of 0 degrees. The regions corresponding to the OIII emission lines near  $\text{H}\beta$  have been masked from the fitting procedure for both sources. Physical parameters of the BLR and scattering regions are found in Table 2. As was already discussed in the previous section, the outer radii of the scatterer region does not change the modelling results

## NGC3783

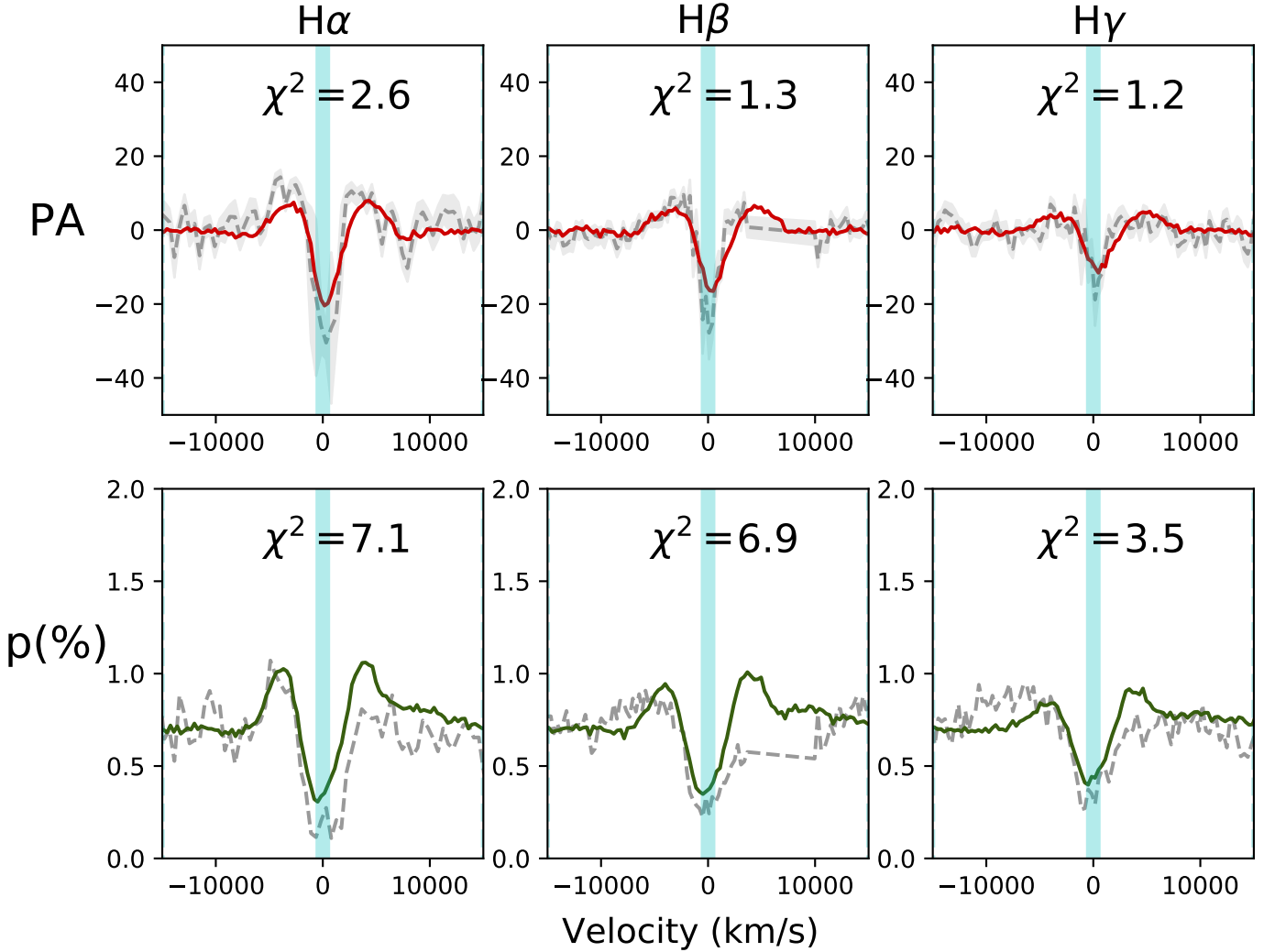


**Figure 7.** Best fit model for NGC3783 PA (top row) and  $p$  spectra (bottom row). Data are shown with gray dashed lines and errors are presented as a gray region around the data. A best fit model corresponds to the model with the best sum of  $\chi^2$  from all fits to H $\alpha$ , H $\beta$  and H $\gamma$ . Data between -15000 and +15000 km/s from the line centers were considered in the fits, with the OIII lines masked out bluewards of H $\beta$ .

significantly as long as the value is at least a few times that of the inner radii and hence are not included in Table 2.

One observational constraint for both, NGC3783 and Mrk 509 is that the level of fractional polarization  $p$  remains relatively constant throughout most of the observed wavelength range (although it shows a slight increase towards the blue in Mrk 509), except below 4000Å where it presents a clear drop, as previously discussed. This means that the height and electron density of the BLR and scattering region cannot vary strongly with radii, otherwise the level of the continuum  $p$  would not stay at the same level, unless opposite effects just cancel each other.

### 4.3 Best fit to NGC 3783

The best fit solutions for the H $\alpha$ , H $\beta$  and H $\gamma$  PA and  $p$  spectra are presented in Figure 7. We adopted the highest BH mass allowed by the derivation of Onken & Peterson (2002) and an inclination angle of 24 degrees, both values in very good agreement with the new estimates by the GRAVITY Collaboration (2021). The reduced  $\chi^2$  is given for each Balmer line and spectrum. The only difference between the modelling of the H $\alpha$ , H $\beta$  and H $\gamma$  emission lines is in their emissivity profiles. They are all characterized by a  $\sim r^{-1/2}$  function but have different starting radii and normalizations. All other parameters defining the BLR and scatterer remained fixed for the best fit model shown in Figure 7.

NGC3783 shows a persistent decrease in the amplitude of the  $M$ -type profiles towards higher transition Balmer

## Mrk509

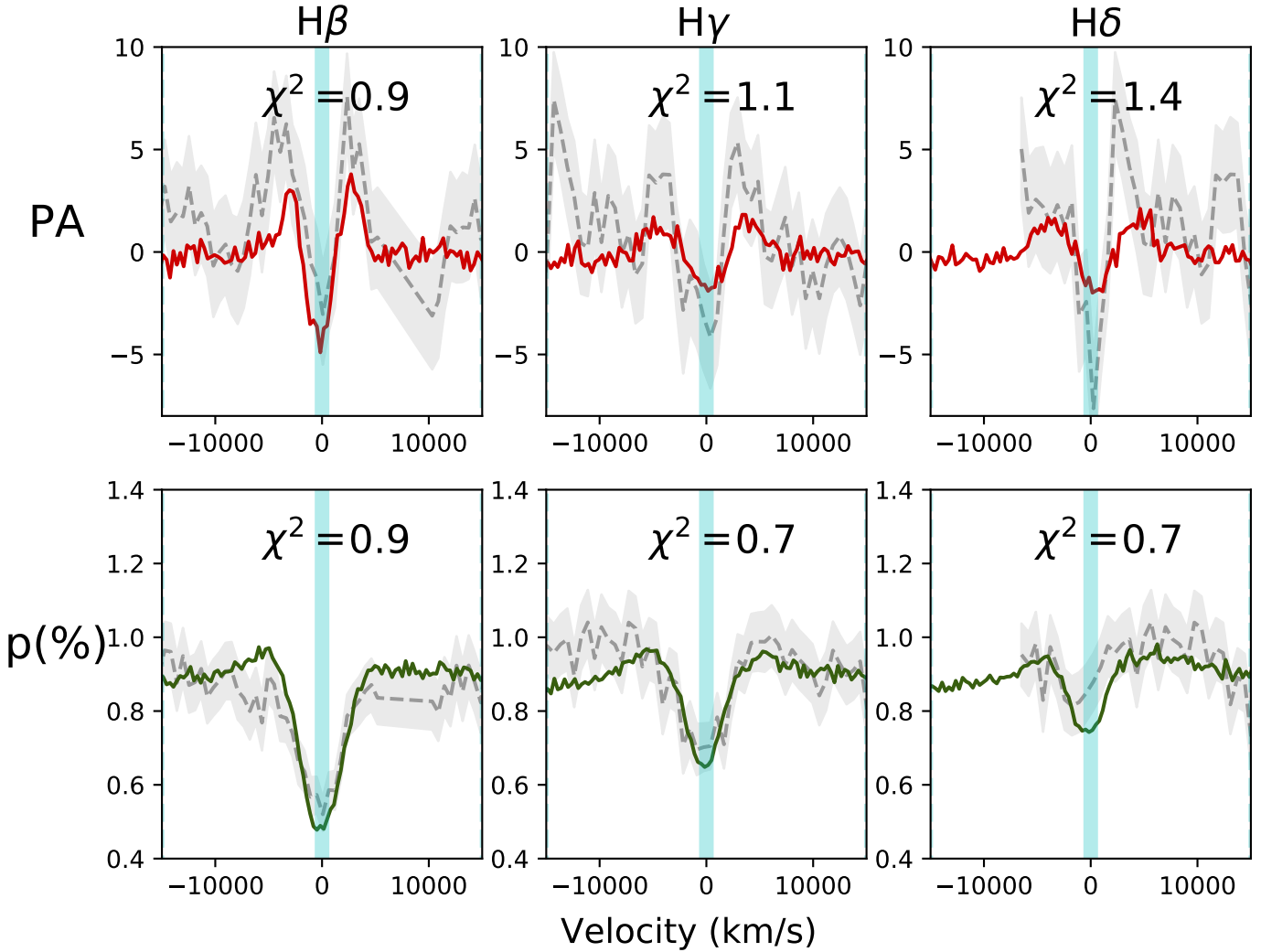


**Figure 8.** Same as Figure 7 but for Mrk509 for the H $\beta$ , H $\gamma$  and H $\delta$  Balmer lines. Notice that the data for this object is of lower signal-to-noise than NGC3783.

lines, as seen in the PA as well as the  $p$  spectra. The shoulders of the  $M$  features also become less sharp. On the other hand, the  $p$  continuum remains largely constant. The main challenge was to find a parameter combination that would yield sufficient  $p$  continuum without too sharp and large shoulders in the PA and  $p$  lines but still a large trough for the PA  $M$  profile.

It is found that a deep trough in the line profiles can be achieved by the combination of a small BH mass and large radial outflows in both, the BLR and scattering medium. The scatterer wind velocity changes from 8000 km/s close to the nucleus to 4000 km/s at 0.03 pc in radius. This profile was modeled as an equally spaced step function with steps of 1000 km/s. The BLR wind velocity was explored in steps of 500 km/s and it did not vary with radius. Gaussian and exponential emissivity profiles were also tested besides the  $\sim r^{-1/2}$  law, but gave poor results. The width of the scattering region is found to be 0.4 times its innermost radius,

although we remind the reader that this width is more representative of the width of an atmosphere around the BLR region than an actual disc width. The innermost radius of the scattering region was found to be 0.003 pc, which corresponds to half of the distance to the accretion disc B-band emission peak, and 2.5 times smaller than the outskirts of the disc as detected in the J-band (Lira et al., 2011), which is also coincident with the RM lag for H $\beta$  (Onken & Peterson 2002). Interestingly, using polarization RM for NGC 4151 it has been shown that the location of the equatorial scatterer is found to coincide with the lag measurements for CIV and H $\beta$  (Gaskell et al. 2012).

In general, the models better reproduce the PA signatures than the structure observed in the  $p$  spectra, in particular the continuum  $p$  in the vicinity of the line. This could be due to the limiting geometrical options available to our modelling, as already discussed above. Besides, no flaring or warping of the Scatterer can be explored. Still, the model

**Table 2.** Best Fit Parameters for NGC 3783 and Mrk 509

| Object / Model Parameter Value   | Observed Value  | Reference               |
|--|---|-------------------------|
| NGC 3783   |   |                         |
| $M_{\text{BH}} = 3.5 \times 10^7 M_{\odot}$  | $2.4 - 3.5 \times 10^7 M_{\odot}$                     | Onken & Peterson (2002) |
| Assumed inclination angle = 24 degrees   | $23_{-10}^{+16}$                                      | GRAVITY (2021)          |
| BLR innermost radius $R_{\text{in}} = 0.003 \text{ pc } (1 \times 10^3 R_{\text{Sch}})$  |   |                         |
| BLR line emissivity profile $\sim r^{-1/2}$  |   |                         |
| BLR peak emissivity radii ( $H\gamma$ , $H\beta$ , $H\alpha$ ) = $4, 6, 10 \times 10^{-3} \text{ pc } (1, 2, 3 \times 10^6 R_{\text{Sch}})$  | $H\beta$ RM results = $6.8 \times 10^{-3} \text{ pc}$ | Onken & Peterson (2002) |
| BLR radial velocity = 2500 km/s  |   |                         |
| BLR and Scatterer height = 0.001 pc ( $335 R_{\text{Sch}}$ )   |   |                         |
| Scatterer innermost radius $R_{\text{in}} = 0.001 \text{ pc } (1 \times 10^3 R_{\text{Sch}})$  |   |                         |
| Scatterer electron density $n_e = 3 \times 10^7 \text{ cm}^{-3}$   |   |                         |
| Scatterer vertical Thompson opacity $\tau = 0.07$  |   |                         |
| Scatterer horizontal Thompson opacity $\tau = 2.0$   |   |                         |
| Mean free path of photons = $0.015 \text{ pc } (5 \times 10^3 R_{\text{Sch}})$   |   |                         |
| Scatterer outflow velocity = 8000 km/s at 0.002 pc; 4000 km/s at 0.035 pc  |   |                         |
| Mrk 509  |   |                         |
| $M_{\text{BH}} = 1.4 \times 10^8 M_{\odot}$  | $1.4 \times 10^8 M_{\odot}$                           | Peterson et al. (2004)  |
| Assumed inclination angle = 24 degrees   |   |                         |
| BLR innermost radius $R_{\text{in}} = 0.02 \text{ pc } (2 \times 10^3 R_{\text{Sch}})$   |   |                         |
| BLR line emissivity profile $\sim r^{-1/2}$  |   |                         |
| BLR peak emissivity radii ( $H\delta$ , $H\gamma$ , $H\beta$ ) = $2, 6, 10 \times 10^{-2} \text{ pc } (2, 6, 10 \times 10^5 R_{\text{Sch}})$ | $H\beta$ RM results = $6.8 \times 10^{-2} \text{ pc}$ | Peterson et al. (2004)  |
| BLR radial velocity = 2000 km/s at 0.02 pc; -1500 km/s at 0.1 pc   |   |                         |
| BLR and Scatterer height = 0.0015 and 0.003-0.005 pc ( $150$ and $300\text{-}500, R_{\text{Sch}}$ )  |   |                         |
| Scatterer innermost radius $R_{\text{in}} = 0.02 \text{ pc } (2 \times 10^3 R_{\text{Sch}})$   |   |                         |
| Scatterer electron density $n_e = 4 \times 10^7 \text{ cm}^{-3}$ at 0.02 pc; $6 \times 10^6 \text{ cm}^{-3}$ at 0.1 pc                       |   |                         |
| Scatterer vertical Thompson opacity (at 0.1 pc) $\tau = 0.05$  |   |                         |
| Scatterer horizontal Thompson opacity $\tau = 3.2$   |   |                         |
| Mean free path of photons (at 0.1 pc) = $0.077 \text{ pc } (8 \times 10^3 R_{\text{Sch}})$   |   |                         |
| Scatterer outflow velocity = 6000 km/s at 0.02 pc; 1000 km/s at 0.15 pc  |   |                         |

follows well the general shape of the troughs and it shows the slight asymmetry observed at the center of the line, particularly in the profiles of  $H\beta$  and  $H\gamma$ .

#### 4.4 Best fit to Mrk 509

The PA and  $p$  line features in Mrk 509 are broader and show less amplitude than those seen in NGC 3783. As already discussed in section 5.1, it would seem that the BH mass would be sufficient to explain the differences in PA profile between NGC 3783 and Mrk 509. However, just as their BH masses differ by a factor of  $\sim 5$ , the location of their BLRs differ by a factor of  $\sim 10$  (Onken & Peterson 2002, Peterson et al. 2004). Normalizing by their Schwarzschild radii, the BLRs are found at  $2 \times 10^3$  and  $7 \times 10^3 R_{\text{Sch}}$  for NGC 3783 and Mrk 509, respectively. As a result, the Keplerian velocities imparted by the BHs at the distance of the BLR formation are rather similar in both objects.

Mrk 509 does not show an  $M$ -type PA profile in  $H\alpha$  (see Figures 2, 4 and 5 and the discussion in Section 3.3). Instead, the shape seems to be somewhat closer to the profile proposed by Smith et al. (2005). In  $H\beta$  a clear  $M$  PA profile is present and the troughs become more and more prominent in higher order Balmer lines. Given the low signal-to-noise of the  $H\alpha$  data, in Mrk 509 we will model the  $H\beta$ ,  $H\gamma$  and  $H\delta$  observed polarized features.

The observations show that while the PA profile seems to show an increase in trough amplitude when moving from  $H\beta$  to higher order Balmer transitions ( $H\gamma$ ,  $H\delta$  and further), the opposite trend is seen in the  $p$  line profile. Unfortunately,

we were not able to find a unique BLR–scatterer model that would reproduce this behaviour. The final model presented in Figure 8 shows a successful fit to the features observed in the  $p$  spectra (continuum level and line features) but which is not able to follow the PA profile changes seen across Balmer lines.

Comparison between our models presented in section 5.1 and the PA profiles in Mrk 509 would suggest that the BLR radial velocity should change from an outflow at the radius where higher order Balmer lines are produced to an inflow at the distance where  $H\alpha$  arises (see Figure 6, panel d). This however, does not take into account that photons are not scattered *in-situ*, but where the optical depth in the scattering medium becomes  $\sim 1$ . Choosing different scatterer electron densities the location where this condition is met can be modified. To obtain the correct  $p$  line profile and  $p$  continuum level, we found that the required parameters are: a  $\rho_e \sim$  a few times  $10^6 \text{ cm}^{-3}$  and a disk height of at least 0.005 pc. Therefore the mean free path of photons along the mid-plane of the scattering disk is  $\sim 0.1 \text{ pc}$  and changes in the velocity field would be smeared within this spatial scale. Since RM results show that all Balmer emission lines should be produced within  $\sim 0.1 \text{ pc}$  from the nucleus in Mrk 509, for  $\rho_e \sim 10^6 \text{ cm}^{-3}$  photons will travel freely from regions characterized by inflowing motions to those characterized by outflowing motions without preserving a characteristic kinematics.

In order to decrease the level of smearing of the distinct kinematics within the BLR and scattering disk, we opted for models where larger electron densities were found

at smaller radii. Hence those regions became more optically thick and photons were scattered closer to the characteristic radius where they were produced. This strategy reduced by about half the characteristic radii inside which higher order Balmer lines were scattered, but it was not effective enough to solve our problem of the mismatch between the behaviour of the PA and  $p$  spectra. MCMC exploration of the parameter space might solve this issue but it is beyond what can be presently done.

The final model is presented in Figure 8. As with NGC 3783, emissivity profiles were described by a  $r^{-1/2}$  law with different starting radii for different Balmer lines. To isolate regions with different kinematics, the starting (and peak) emissivity for H $\beta$  was chosen to be 0.1 pc, slightly larger than the 0.06-0.08 pc determined from RM results. The scatterer density decreases from  $4 \times 10^7 \text{ cm}^{-3}$  at 0.02 pc to  $6 \times 10^6 \text{ cm}^{-3}$  at 0.1 pc and it stays constant at larger radii. The BLR radial velocity also varies from an outflow of 2000 km/s in the inner part to an inflow of -1500 km/s at 0.1 pc. The scatterer, on the other hand, always presents an outflowing radial motion with speeds of 6000 km/s in the inner part and reaching a velocity of 1000 km/s at  $\sim 0.15$  pc. Keeping the scatterer and BLR compact ( $< 0.15$  pc) resulted in less pronounced shoulders around the  $p$  profile. The typical width of the scattering region is found to be 0.2 times its innermost radius, half the value found for NGC 3783.

## 5 DISCUSSION

One of the most remarkable results from our spectropolarimetric observations is the change in the line profiles along the Balmer sequence, as observed in Mrk 509. This clearly reinforces the notion that the BLR is an extended source and that physical and dynamical conditions can rapidly change with radius in AGN nuclei. Furthermore, it demonstrates that powerful nuclear winds might exist in many Seyfert galaxies but their presence might only be revealed by observing high order Balmer lines in polarized light.

The signatures of inflows and particularly outflows have been found in many AGN. Their presence is also invoked by numerical simulations that require the AGN to modulate the star formation rate in their host galaxies (e.g., Harrison 2017, Veilleux et al. 2020), as well as holistic models of the AGN phenomenology (Elvis 2000, 2017). The so-called Warm Absorbers represent one of the most commonly observed nuclear winds: photoionized gas distances of  $\sim 1 - 1000$  pc, outflowing with velocities of hundreds of km/s, are detected in the UV and X-ray spectra of  $\sim 50\%$  of Seyfert nuclei (Crenshaw & Kraemer 1999). Nuclear winds with more extreme properties, detected much closer to the accretion disk and with velocities of thousands of km/s, have been observed in only a few sources such as NGC 5548 (Kaastra et al. 2014), NGC 985 (Ebrero et al. 2016), Mrk 335 (Longinotti et al. 2019) and NGC 3783 (Mehdipour et al. 2017, Kriss et al. 2019). They have been interpreted as clumpy outflows associated to the accretion disk (Laha et al. 2021), however, their exact nature remains unclear. The scarcity of these results might change with further spectropolarimetric observations of Seyfert 1 nuclei,

while the larger collective area of future 30m-class telescopes will be able to probe this in many nearby AGN.

We have also shown that the modelling of the data obtained for NGC 3783 and Mrk 509 offers the opportunity to put significant constraints into the properties of these two sources. Even though we have not been able to fully explore the parameter space that governs the emission from these nuclei, and our models still suffer from many simplifications, we have shown that nuclear high-velocity winds are necessary to explain the observations. Our exploration of the parameter space demonstrate that variations in geometrical and dynamical quantities that characterize the BLR and the scatterer leaves a clear imprint in the PA and  $p$  spectra. Besides, as already discussed in Savić et al. (2018) and Lira et al. (2020), the modelling shows that in the absence of a strong radial wind the profile of the lines seen in spectropolarimetric observations reverts to that proposed by Smith et al. (2002, 2004, 2005).

As already mentioned, recent Swift, XMM-Newton, NuSTAR and HST observations of NGC 3783 have detected the presence of a nuclear wind in this source from the follow up of an obscuring event taking place in December 2016 (Mehdipour et al. 2017). The event allowed for the findings of several new absorption features that revealed the existence of outflowing material with velocities of a few thousand km/s at distance of about 10 light days ( $\sim 10^{-3}$  pc), in excellent agreement with the results from our STOKES modelling. The changing features in the spectropolarimetric observations of Mrk 509 also demonstrate that these winds might be transient phenomena. Obscuring events such as the one observed in NGC 3738 are extremely rare, and reinforces the idea that spectropolarimetry might be the best tool to search for powerful nuclear winds in AGN.

## 6 DATA AVAILABILITY STATEMENTS

The raw data underlying this article can be downloaded from the ESO Archive. The processed data will be shared on reasonable request to the corresponding author.

## ACKNOWLEDGMENTS

PL acknowledges funding from Fondecyt Project #1201748. MK acknowledges support from JSPS grant 20K04029.

## REFERENCES

- Afanasiev V. L., Popović L. Č., Shapovalova A. I., 2019, MNRAS, 482, 49
- Afanasiev V. L., Amirkhanyan V. R., 2012, AstBu, 67, 438. doi:10.1134/S1990341312040074
- Antonucci R., 1988, *smbh.proc*, 26, *smbh.proc*
- Antonucci R. R. J., 1984, ApJ, 278, 499
- Bentz M. C., Katz S., 2015, PASP, 127, 67
- Bentz M. C., et al., 2010, ApJ, 716, 993
- Cardelli J. A., Clayton G. C., Mathis J. S., 1989, ApJ, 345, 245
- Crenshaw D. M., Kraemer S. B., 1999, ASPC, 175, 341
- Ebrero J., Kriss G. A., Kaastra J. S., Ely J. C., 2016, A&A, 586, A72



- Elvis M., 2000, *ApJ*, 545, 63  
 Elvis M., 2017, *ApJ*, 847, 56  
 Ferland G. J., Netzer H., Shields G. A., 1979, *ApJ*, 232, 382  
 Ferland G. J., Peterson B. M., Horne K., Welsh W. F., Nahar S. N., 1992, *ApJ*, 387, 95  
 Fossati L., Bagnulo S., Mason E., Landi Degl’Innocenti E., 2007, *ASPC*, 364, 503  
 Gaskell C. M., Goosmann R. W., Merkulova N. I., Shakhovskoy N. M., Shoji M., 2012, *ApJ*, 749, 148  
 Goodrich R. W., Miller J. S., 1994, *ApJ*, 434, 82  
 GRAVITY Collaboration, Amorim A., Bauböck M., Brandner W., Bolzer M., Clénet Y., Davies R., et al., 2021, arXiv:2102.00068  
 Harrison C. M., 2017, *NatAs*, 1, 0165  
 Hoffman J. L., Chornock R., Leonard D. C., Filippenko A. V., 2005, *MNRAS*, 363, 1241  
 Kaastra J. S., Kriss G. A., Cappi M., Mehdipour M., Petrucci P.-O., Steenbrugge K. C., Arav N., et al., 2014, *Sci*, 345, 64  
 Kishimoto M., Antonucci R., Blaes O., 2003, *MNRAS*, 345, 253  
 Kishimoto M., Antonucci R., Boisson C., Blaes O., 2004, *MNRAS*, 354, 1065  
 Kriss G. A., Mehdipour M., Kaastra J. S., Rau A., Bodensteiner J., Plesha R., Arav N., et al., 2019, *A&A*, 621, A12  
 Laha S., Reynolds C. S., Reeves J., Kriss G., Guainazzi M., Smith R., Veilleux S., et al., 2021, *NatAs*, 5, 13  
 Lamy H., Hutsemékers D., 2000, *A&AS*, 142, 451  
 Landi Degl’Innocenti E., Bagnulo S., Fossati L., 2007, *ASPC*, 364, 495  
 Lira P., Goosmann R. W., Kishimoto M., Cartier R., 2020, *MNRAS*, 491, 1  
 Lira P., Arévalo P., Uttley P., McHardy I., Breedt E., 2011, *MNRAS*, 415, 1290  
 Longinotti A. L., Kriss G., Krongold Y., Arellano-Cordova K. Z., Komossa S., Gallo L., Grupe D., et al., 2019, *ApJ*, 875, 150  
 Marin F., Goosmann R. W., Gaskell C. M., 2015, *A&A*, 577, A66  
 Marin F., Goosmann R. W., Gaskell C. M., Porquet D., Dovčiak M., 2012, *A&A*, 548, A121  
 Mehdipour M., et al., 2017, *A&A*, 607, A28  
 Miller J. S., Robinson L. B., Goodrich R. W., 1988, *igbo.conf*, 157, *igbo.conf*  
 Onken C. A., Peterson B. M., 2002, *ApJ*, 572, 746  
 Pancoast A., Brewer B. J., Treu T., Park D., Barth A. J., Bentz M. C., Woo J.-H., 2014, *MNRAS*, 445, 3073  
 Peterson B. M., et al., 2004, *ApJ*, 613, 682  
 Reichert G. A., et al., 1994, *ApJ*, 425, 582  
 Rojas Lobos P. A., Goosmann R. W., Marin F., Savić D., 2018, *A&A*, 611, A39  
 Savić D., Goosmann R., Popović L. Č., Marin F., Afanasiev V. L., 2018, *A&A*, 614, A120  
 Savić D., Popović L. Č., Shablovinskaya E., Afanasiev V. L., 2020, *MNRAS*, 497, 3047  
 Schmid H. M., Appenzeller I., Camenzind M., Dietrich M., Heidt J., Schild H., Wagner S. J., 2000, *SPIE*, 4005, 264, *SPIE.4005*  
 Schmidt G. D., Smith P. S., 2000, *ApJ*, 545, 117  
 Smith J. E., Robinson A., Alexander D. M., Young S., Axon D. J., Corbett E. A., 2004, *MNRAS*, 350, 140  
 Smith J. E., Young S., Robinson A., Corbett E. A., Giannuzzo M. E., Axon D. J., Hough J. H., 2002, *MNRAS*, 335, 773  
 Stirpe G. M., et al., 1994, *ApJ*, 425, 609  
 Tran H. D., 1995, *ApJ*, 440, 597  
 Veilleux S., Maiolino R., Bolatto A. D., Aalto S., 2020, *A&ARv*, 28, 2  
 Young S., Corbett E. A., Giannuzzo M. E., Hough J. H., Robinson A., Bailey J. A., Axon D. J., 1999, *MNRAS*, 303, 227

## APPENDIX A: Q AND U SPECTRA

Total flux and unnormalized Q and U ISP-uncorrected spectra are presented in Figure A1. The zero level is shown in the Q and U figures with a gray line.

The Q spectrum of NGC 3783 and U spectrum of Mrk 509 show strikingly clear the coincidence of strong changes in polarized flux at the position of the full Balmer series.

## APPENDIX B: BEST-FIT RESULTS IN Q AND U SPACE

In the same manner that the PA spectral continuum level was taken to zero degrees in order to be compared with model results in Section 4.2, the  $q$  and  $u$  spectra were *rotated* so that the continuum level in the  $u$  spectra corresponded to zero flux (e.g., Landi Degl’Innocenti, Bagnulo & Fossati, 2007). These new spectra are denoted as  $q'$  and  $u'$ .

The  $q'$  and  $u'$  spectra for NGC 3783 and Mrk 509 are shown in Figures B1 and AB, respectively. The fractional fluxes are expressed in percentage. For NGC 3783  $q'$  and  $u'$  look remarkably similar, while for Mrk 509 the  $q'$  spectrum shows more strongly polarized lines and more symmetric profiles than the  $u'$  spectrum.

The best-fit models to the  $q'$  and  $u'$  spectra are overplotted and the best-fit  $\chi^2$  values for each line are shown in the subpanels. NGC 3783 presents rather high values of  $\chi^2$  and several wiggles seen in the data are not seen in the model and viceversa. This could be due to non-negligible atmospheric depolarization (Section 2.3), a non-perfect rotation of the  $q$  and  $u$  spectra, and shortcomings in our modelling capabilities, among other. The lower signal-to-noise data for Mrk 509 results in lower  $\chi^2$  values.

This paper has been typeset from a  $\text{\TeX}/\text{\LaTeX}$  file prepared by the author.

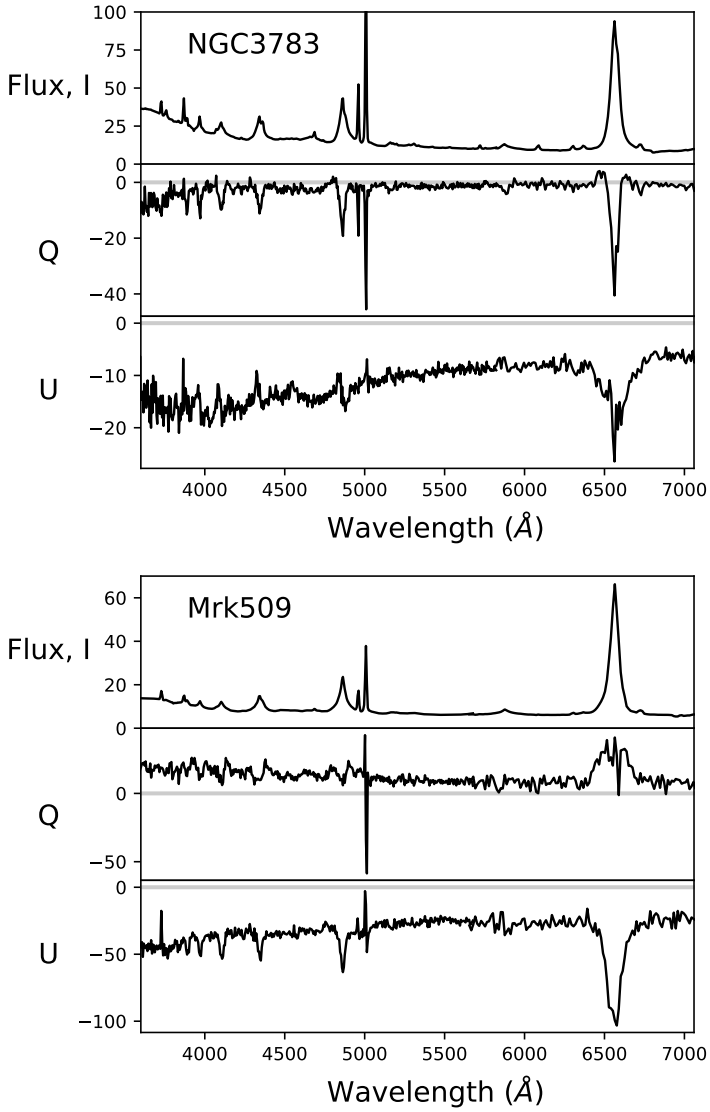


**Figure A1.** Total flux and unnormalized Q and U ISP-uncorrected spectra for NGC 3783 (top) and Mrk 509 (bottom). The  $I$  spectra is presented in units of  $10^{-15}$  erg/s/cm<sup>2</sup>/Å while the Stokes spectra are shown in units of  $10^{-17}$  erg/s/cm<sup>2</sup>/Å for both objects.

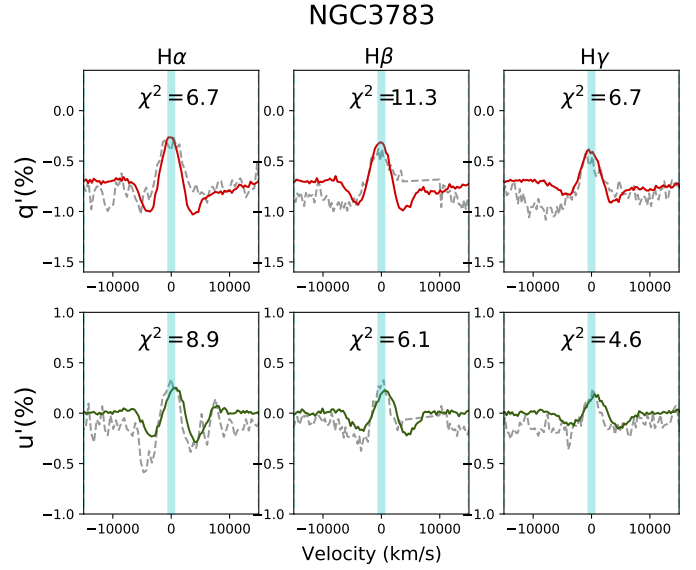


**Figure B1.** Best fit model for NGC 3783  $q'$  and  $u'$  spectra (top and bottom row, respectively). Data are shown with gray dashed lines and errors are presented as a gray region around the data. A best fit model corresponds to the model with the best sum of  $\chi^2$  from all fits to H $\alpha$ , H $\beta$  and H $\gamma$ . Data between -15000 and +15000 km/s from the line centers were considered in the fits, with the OIII lines masked out bluewards of H $\beta$ .

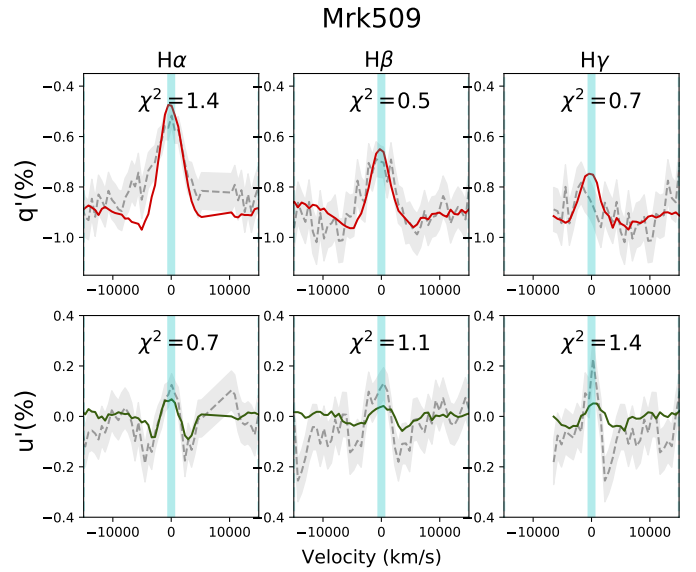


**Figure B2.** Same as Figure B1 but for Mrk 509 showing the  $q'$  and  $u'$  spectra and modelling for the H $\beta$ , H $\gamma$  and H $\delta$  Balmer lines.